Radiometric correction of multispectral images collected by a UAV for phenology studies

Karl Adler

2018

Department of

Physical Geography and Ecosystem Science

Lund University

Sölvegatan 12

Karl Adler (2018).
Radiometric correction of multispectral images collected by a UAV for phenology studies
Master degree thesis, 30 credits in *Physical Geography and Ecosystem Analysis*
Department of Physical Geography and Ecosystem Science, Lund University

Level: Master of Science (MSc)

Course duration: *January* 2018 until *June* 2018

Disclaimer

This document describes work undertaken as part of a program of study at the University of Lund. All views and opinions expressed herein remain the sole responsibility of the author, and do not necessarily represent those of the institute.

Radiometric correction of multispectral images collected by a UAV for phenology studies

Karl Adler

Master thesis, 30 credits, in *Physical Geography and Ecosystem Analysis*

Per-Ola Olsson
Lund University

Lars Eklundh
Lund University

Exam committee:
Hongxiao Jin, Lund University
Andreas Persson, Lund University

Abstract

Vegetation monitoring over time is important in a changing world due to climate change. Remote sensing, especially with the use of unmanned aerial vehicles (UAV), can be utilized to monitor vegetation at flexible scales at an accurate degree. However, the relatively new remote sensing platforms that are UAVs imply the requirement of understanding how to best monitor vegetation in an accurate way with the system in mind. This study aims to test a method for the radiometric calibration of images captured by a Parrot Sequoia multispectral camera to derive reflectance images. The radiometric correction method was tested and evaluated against Spectralon reflectance plates and in-situ normalized difference vegetation index (NDVI) during a field campaign. The technical properties of the camera were tested during different experiments to determine what factors propagate to the product reflectance images. The results show that the radiometric correction method could produce accurate estimates of Spectralon reflectance plates. However, not all Spectralon reflectance plates can be accurately estimated. The calculated NDVI from the UAV in the field after a radiometric calibration was far closer to the NDVI derived from the handheld spectrometer. The technical properties and thus limitations of the camera can be rectified by to a certain degree by radiometric calibration and pre-processing method used. However, more accurate reflectance estimates require a rigorous pre-processing of the data used to derive the radiometric calibration.

Keywords: Physical Geography, UAV, Radiometric Correction, Multispectral Camera, Reflectance.

Table of contents

1   Introduction

The technological advances in unmanned aerial vehicles (UAV) have been providing the possibilities of acquiring data in various fields of vegetation monitoring (Yang et al. 2017). One such field is phenology. Phenology is the science related to biological entities periodic phenomena to climatic conditions such as plant growth start and ending during a year (Klosterman & Richardson, 2017). Plant phenology governs ecosystem functions such as carbon sequestration that affect the climate and food security (Klosterman & Richardson, 2017; Xue & Su, 2017). With prospects of climate change the need to understand plant phenology becomes more important (Richardson et al. 2009).

The two most common methods for gathering of phenological data are in-situ measurements and remotely sensed data (Richardson et al. 2009). Remote sensing provides benefits over in-situ measurement as remote sensing can provide a large spatial scale representation, variability in sensor payload and sampling of hard to reach areas (Chuvieco, 2016). Remote sensing can be done with a satellite or a near-surface camera where both options provide positive and negative factors. For satellites a problem is the low spatial resolution, clouds blocking the view and other atmospheric effects that need to be taken care of (Klosterman et al. 2018; Klosterman & Richardson, 2017). Near-surface cameras have problems associated with the lack of landscape representation, only seeing what is directly in front of the system thus obstructing background vegetation that might differ resulting in a false view of the vegetation (Klosterman et al. 2018; Klosterman & Richardson, 2017). These negative aspects provide problems when conducting phenology studies that could be rectified by utilizing a method representing the vegetation at an intermediate scale between the satellite and near-surface cameras (Klosterman & Richardson, 2017; Klosterman et al. 2018).

The use of unmanned aerial vehicles (UAV) fills the gap between large-scale satellite and small-scale near-surface remote sensing options. High potential temporal resolution, low cost of the platform and high spatial resolution are some of the key points when using a UAV (Berra et al. 2016). Several studies have collected phenological data from a UAV successfully with mounted red, green and blue (RGB) cameras (Berra et al. 2016; Klosterman et al. 2018; Klosterman & Richardson, 2017). However, Burkart et al. (2017) argue that more accurate phenological data will require more wavelength bands such as near-infrared (NIR) and especially with proper radiometric calibration. This topic of radiometric calibration is reoccurring in many of the studies which is the method for deriving reflectance values from the digital numbers of the pixels provided by the sensor in question (Chuvieco, 2016). Furthermore, the radiometric calibration methods used often do not include changes in illumination. For example, Berra et al. (2016) argue that the changes in illumination for between each flight is by some degree compensated by their post-processing of the sensor data but

however by no means provides an ultimate solution to the problem. Yang et al. (2017) further conclude that there is a lack of radiometric calibrated cameras used with UAV's hence neglecting the true reflectance of the vegetation and only dealing with raw digital numbers. This emphasize the need to use a robust method for radiometric correction with a radiometric calibrated camera that takes in to account the incoming solar radiation and not just the radiance from the surface. All this to have reflectance data of vegetation that is valid and comparable in time regardless of illumination conditions.

2 Aim

New sensor technologies arriving for use with UAVs in phenology is constantly emerging with promises to the end user. However, to collect data for phenological studies, scientific evaluations of the hardware used and the methods applied are required to produce robust data that can be comparable over time. Hence, this study aims to:

- Develop a radiometric correction method for lightweight multispectral cameras with a sunshine sensor.
- Quantify the sources of errors that are present in images collected with the Parrot Sequoia system.
- Perform radiometric correction on images captured with a Parrot Sequoia camera and evaluate against field measured NDVI.

3 Background

3.1 Remote sensing and phenology

There are many options to gather phenological data with remote sensing. However, some aspects need to be fulfilled regardless of platform and sensors. To derive the amount of vegetation and its status for instance for a given time there is a need to use a measurable metric to observe changes. The most basic metric to use is the reflectance of the vegetation, the ratio of outgoing radiation (radiance) and incoming radiation (irradiance) to observe vegetation activity from passive sensors (Chuvieco, 2016. P.346-348). The premise lies within the notion that the reflectance for a specific electromagnetic wavelength, the spectral reflectance, of vegetation changes due to factors such as plant type, water content, chlorophyll content and morphology to name a few (Xue & Su, 2017). There might, however, be a need to compare metrics more linked to biophysical variables rather than spectral reflectance. For this vegetation indices (VI) are often applied where two or more wavelength bands are used in an equation to compute the VI in question (Chuvieco, 2016. P.269). Furthermore, VIs can help minimize problems associated with raw reflectance data such as changes in viewing angles, atmospheric distortions and shadows when the VI is ratio based (Chuvieco, 2016. P.269).

Different VI use different wavebands and provide information about different biophysical variables (Xue & Su, 2017; Yang et al. 2017). For example, one of the more commonly used VIs is the normalized difference vegetation index (NDVI) (Xue & Su, 2017). NDVI utilizes the chlorophyll absorbing red and the non-absorbing NIR waveband and is correlated to e.g. measured leaf area index (LAI) and biomass for example (Xue & Su, 2017; Yang et al., 2017):

$$NDVI = \frac{(NIR - Red)}{(NIR + Red)} \quad eq.\,1$$

where *NDVI* is the output index value ranging from -1 to 1 with a value close to 1 corresponding to high amount of vegetation, *NIR* is the near-infrared waveband reflectance or signal and *Red* is the red waveband reflectance or signal. As can be seen due to the nature of the index it can be calculated by using reflectance or non-physical counts for the wavebands.

Another example where a VI can provide biophysical information is the study by Richardson et al. (2009) where the green excess index (GEI) was used which compromises of the red, blue and green waveband. Their results showed that measured gross primary product (GPP) in a deciduous forest was significantly correlated with GEI (Richardson et al. 2009). Thus, a VI can be used as a proxy for measurable biophysical variables that are of importance when assessing the phenology of a specific location or plant.

Phenology analysis in remote sensing is commonly performed at a pixel-by-pixel basis which imposes two specific requirements that are geometric rectification and radiometric calibration to discern true change from false (Chuvieco, 2016). The geometric accuracy involves that the pixels present in two images represent the same ground features. A way to obtain a good geometric match between two images is to use common control points present in both images, that are invariant features present in both images, to make sure the right pixels are overlapping (Chuvieco, 2016. P.343-345). However, a radiometric consistency must be present between the images which is obtained with a radiometric calibration of the sensor in question (Chuvieco, 2016. P.345-346). The radiometric calibration refers to the conversion of raw digital values captured by the sensor to the physical unit of reflectance (Chuvieco, 2016. P.345-346). When comparing raw digital values between images, if different, might provide indications of change where there are none due to various environmental changes for instance such as changes in illumination (Chuvieco, 2016. P.345-346). Further, if common control points are to be chosen within a time series it will rely on that the point in question has a uniform reflectance i.e. that they stay invariant if the surface in question is not changed– this raises the importance of having proper radiometric ally calibrated camera (Rasmussen et al. 2016).

3.2 UAV remote sensing

Zhang et al. (2017) showed that the usage of UAV platforms has soared in popularity in the timespan from the years 2010-2015. The benefits of using UAV's for remote sensing are evident with the small formfactor, relative low cost, flexible payload which has been proven to work for many remote sensing applications (Zhang et al. 2017). UAV platforms have proven to be very useful as the flight altitude of an UAV is often so low that no atmospheric effects need to be considered such as aerosol content in the analysis, hence some radiometric corrections required for satellite data can be neglected when using an UAV (Yang et al. 2017). However, a disadvantage with UAV images is the need to acquire data with similar illumination condition. For example, the bi-directional reflectance direction function (BRDF) is a small factor for satellite remote sensing but is amplified for UAV remote sensing (Stark et al., 2018). A non-uniform illumination upon the scene can result in dark or bright hotspots depending on viewing and solar angle which is reduced on larger scales (Stark et al. 2018). Hence, some conditions must be controlled such as solar intensity, UAV orientation in relation to the sun and uniform cloud conditions for each flight (Rasmussen et al. 2016; Berra et al. 2017; Burkart et al. 2017; Klosterman & Richardson 2017). Apart from these environmental factors on radiometric quality there are more technical factors that also need to be controlled over time that affect measured reflectance. In several articles the settings of the sensors are kept uniform over time such as exposure and ISO (Klosterman & Richardson 2017; Klosterman et al. 2018; Rasmussen et al.

2016; Berra et al. 2017). Due to these environmental and technical factors Yang et al. (2017) states that there is a lack of standardized methodology for UAV remote sensing.

In the case of payload and methodology the notion of commercial off the shelf cameras (COTS) are common in the literature. The use of COTS on UAV platforms indicate low costs with a possibility to create phenological data (Berra et al. 2016; Berra et al. 2017; Burkart et al. 2018). However, these COTS systems lack multispectral capability as the commercial cameras often only have a red, green and blue channel that limit the analytical possibilities of the system (Xue & Su, 2017; Yang et al. 2017). However, the vegetation indices possible to create with RGB data have been proven to be possible and successful in the study by Burkart et al. (2017) and Berra et al. (2016) to a certain degree.

3.3   Radiometry and remote sensing phenology

The case of radiometric calibration with UAV remote sensing differs from study to study. The examples mentioned above does not rely on using a radiometric calibrated camera for several reasons. One method can be seen in Berra et al. (2016) where the camera is set to static settings that will not change over time thus making comparable time series possible. Another method also shown in Berra et al. (2016) is that the vegetation index used in their case does not rely on reflectance data but merely the digital counts of the Red, Green and Blue channel in the camera – the ratio between the bands. However, Berra et al. (2016) does conclude that the vegetation index used takes no proper regard for varying illumination conditions that results in unwanted index variation. In the article by Burkart et al. (2017) they utilized reflectance panels for each flight and analysed the digital values present within these panels to determine if their digital values were stable over time. Furthermore, they discarded images where these reflectance panels had values that were out of the normal range of values (Burkart et al. 2017).

However, when it comes to having phenological data that are accurate regardless of illumination conditions then a radiometric calibration of the camera in use must be done. The most popular method is the empirical line calibration proposed by Smith & Milton (1999). This method has been applied to COTS RGB cameras as well as multispectral cameras with success (Berra et al. 2017; Bueren et al. 2015). The empirical line method requires in-situ measured reflectance of dark and bright objects present in the UAV image. Then a linear relationship is made from these dark and bright objects between measured reflectance and digital numbers (DN) to predict reflectance of other objects present (Smith & Milton, 1999). Thus, measurements of reflectance plates in the field with varying intensity are used to derive a linear relationship to derive a calibration coefficient to be applied on all pixels in an image (Bueren et al. 2015). Due to the structure of the method the

calibration images generally need to be taken with each flight with accompanying field measurements to accommodate for the specific illumination conditions. In the article by Bueren et al. (2015) they argue that unwanted reflectance variability in their results was due to them only taking a single calibration image for their flight. Furthermore, their results show that in longer wavelengths the field measured reflectance could be as much as 1.5 times higher than that of the reflectance acquired from the UAV (Bueren et al. 2015). Additional problems associated with the empirical line method are that it assumes no illumination differences in the image, uniform atmospheric effects across the image and that the surface consists of Lambertian reflections (Smith & Miltion, 1999). These assumptions can be hard to fulfil with UAV flights as cloud cover might vary across the flight and that surfaces in the world tend not to be perfectly Lambertian thus exhibit bi-directional reflectance properties. More radiometric calibration methods are mentioned to be used in UAV remote sensing but at a far less rate as mentioned by Yang et al. (2017) such as the darkest target method, flat field model and internal mean method to name a few.

Incoming solar irradiation is commonly not measured by the UAV platform so that the reflectance calculated is rarely the ratio of radiance and irradiance. Jin & Eklundh (2015) argue that having proper reflectance data derived from radiance and irradiance can provide greater analytical possibilities compared to only using radiance. Their argument stems in the fact that having reflectance data can provide possibilities to create non-ratio-based VI's, thus broadening the capabilities of analysis of the data (Jin & Eklundh 2015). Since there are few UAV mounted cameras with a sunshine sensor there is no common method used to radiometrically calibrate them. Hence, methods used to radiometrically calibrate sensor pairs for measuring reflectance need to be adapted as the one proposed in Jin & Eklundh (2015).

3.4 Camera performance theory

The performance and characteristics of the camera has an impact on output data in remote sensing (Kelcey & Lucieer, 2012). Therefore, it is necessary to quantify certain aspects of the camera that propagate to the output. In the article by Kelcey & Lucieer (2012) they present the general components that make up the measured digital value in an equation that goes as follows:

$$DN_{RAW} = DN_{rad} \times FT_{lambda} \times ME_{lambda} \times V_{LUT(i,j)} + (DN_{sn} + DN_{rn}) \quad eq.\,2$$

where DN_{RAW} is the output digital value present in each pixel, DN_{rad} is the actual radiance in digital values, FT_{lambda} is the transmittance of the spectral bandpass filters present in each sensor where a transmittance of 100% equals 1, ME_{lambda} is the monochromatic response/spectral sensitivity which states the required proportion of incoming radiance required to generate an electric charge in the sensor, $V_{LUT(i,j)}$ is the vignetting factor for a pixel which is the potential light intensity falloff or

increase from the centre of the image to the periphery where *i,j* is the pixel in question, DN_{sn} is the systematic noise present in the image such as pixels with values considered as outliers and lastly DN_{rn} which is the random noise present in the image (Kelcey & Lucieer, 2012). From equation 2 it can thus be argued that the technical characteristics of the camera need to be understood to derive accurate data for use in phenology.

3.4.1   Noise

As outlined in Kelcey & Lucieer (2012) noise can be divided in to two parts. One is of a random nature and the other systematic. The random noise is non-reproducible and non-correlated thus making it hard to quantify and be dealt with (Kelcey & Lucieer, 2012). The systematic noise is more consistent which could be a general value bias present in all pixels or in hotspots that is easier to identify and to compensate for (Mullekin et al. 1994; Kelcey & Lucieer, 2012).

Commonly the systematic noise is dealt with by subtracting a dark offset image from the image to be used for deriving reflectance (Berra et al. 2017). A dark offset image refers to the phenomena called dark current which is the production of electrons per pixel from thermal energy (Mullekin et al., 1995). The dark offset image is an image taken with zero incoming solar radiation, like in a pitch-black room, thus only leaving the noise in the sensor providing a "base" DN (Berra et al., 2017). The random noise present is different from image to image and thus subtracting a "dark" image will not suffice. The most common method to deal with the random noise is to apply reductive techniques as a filter upon the image to smooth the values out across the image (Kelcey & Lucieer, 2012). Mansouri et al. (2005) show that dark offset images used need to be made with the same shutter speed and temperature of the sensor as in the field for a proper systematic noise correction. For instance, a dark offset image produced with a specific shutter speed and temperature is not recommended to be used for subtraction for an image taken with another shutter speed and temperature (Mansouri et al., 2005).

3.4.2   Vignetting

Vignetting is the radial decrease or increase in DN values from the image centre (Kelcey & Lucieer, 2012). As shown by equation 2 the effects need to be rectified on a pixel-by-pixel basis. Several dedicated methods exist that can rectify vignetting such as the flatfield method (Mansouri et al, 2005). This method relies on taking an image on a geometric and radiometric uniform surface to create a pixel-by-pixel correction factor to later be applied to subsequent images (Kelcey & Lucieer, 2012).

Apart from the more physical based correction of the flatfield method there are optical modelling approaches to rectify vignetting (Kelcey & Lucieer, 2012). However, Kelcey & Lucieer (2012) mentions

that the implementation of optical models is often more complicated and not necessarily more accurate than physical based approaches such as the flatfield method.

4 Methodology

4.1 Multispectral camera properties

In this study the Parrot Sequoia multispectral camera (Parrot SA, Paris, France) was used. The camera has 4 separate sensors which are in the Green (530-570nm), Red (640-680nm), Red-edge (REG) (730-740nm) and NIR (770-810nm) wavelength bands– all with a global shutter capturing images with a resolution of 1280x960 pixels in a RAW format later saved as .TIFF files. Additionally, there is an RGB sensor with a rolling shutter of 3264x4896 pixels. The camera is also equipped with an optional sunshine sensor that measures incoming solar radiation with 4 sensor that have the same spectral waveband as the 4 separate sensors on the camera. In this study the camera captured images at a radiometric resolution of 10-bit and the sunshine sensor at 16-bit. When an image is captured by the camera there are a total of 9 reading done by the sunshine sensor. Hence, there is information stored as tags within the image as an EXIF or XMP format. EXIF and XMP is information stored within images that contain camera system diagnostics which need to be decoded such as sunshine sensor readings, shutter speed, ISO, dark offset value and temperature to name a few.

Detailed information regarding the monochromatic response/spectral sensitivity and the filter transmittance is not provided, at this moment, by the manufacturer or is insufficient. Hence correction of these are not explicitly taken in to account in this study.

The Parrot Sequoia cameras settings can be set for the 4 individual camera sensors as well as the RGB sensor. Settings that can be altered are ISO and shutter speed. However, the settings of the sunshine sensor cannot be altered. The modifications in this study are done by communication with the Parrot Sequoia over HTTP via Python (http://developer.parrot.com/docs/sequoia/#http-control-api).

4.2 Radiometric Calibration methodology

The Parrot Sequoia was radiometrically calibrated according to the method proposed for dual sensor pair calibration in Jin & Eklundh (2015). The method revolves around radiometrically calibrating a pair of sensors by using the sun as the illumination source (Jin & Eklundh, 2015). The radiometric calibration is done by having an upwards sensor registering incoming radiation and a downward looking sensor fixated upon a reflectance plate registering outgoing radiation. The equation for the radiometric calibration goes as follows:

$$R = \frac{R_L}{k} \times \frac{V_{2obs}}{V_{1obs}} \quad eq.3$$

Where R is the wavelength specific reflectance, R_L is the wavelength specific reflectance of the reflectance plate used in the calibration for the downward looking sensor, V_{2obs} is the downward

looking sensor reading, V_{1obs} is the upward looking sensor reading and k being the slope of the linear relationship between V_{2obs} and V_{1obs} with V_{1obs} as the predictor. However, in this study reflectance is calculated at a pixel-per-pixel basis of the image thus resulting in a slight modification of equation 4:

$$R_{(i,j)} = \frac{R_L}{k_{(i,j)}} \times \frac{V_{2obs(i,j)}}{V_{1obs}} \quad eq.\,4$$

Where $R_{(i,j)}$ is the wavelength specific reflectance of the specific pixel at row i and column j, R_L is the reflectance of the reflectance plate used in the calibration, $V_{2obs(i,j)}$ is the DN value of the pixel at row i and column j, V_{1obs} is the upward looking sensor reading and $k_{(i,j)}$ being the being the slope of the linear relationship between $V_{2obs(i,j)}$ and V_{1obs} at the same pixel row i and column j with V_{1obs} as the predictor. It should be noted that in this study a radiometric calibration refers to a relative radiometric calibration as no radiometric sensitivities are derived.

A reflectance correction matrix from the first term in equation 4 can be created that is dependent on the reflectance plate used for calibration. Thus, each pixel will have its own reflectance correction factor for each band. For example, if a radiometric calibration is done with a 50% reflectance plate then R_L and $k_{(i,j)}$ will be a product of this reflectance plate – creating 50% reflectance plate calibration data. Then this reflectance correction matrix, that is the product of R_L divided by $k_{(i,j)}$, can be applied upon $V_{2obs(i,j)}$ and V_{1obs} from images acquired in the field to produce a reflectance image resulting in:

$$R_{(i,j)} = Ref_{(i,j)} \times \frac{V_{2obs(i,j)}}{V_{1obs}} \quad eq.\,5$$

where $Ref_{(i,j)}$ is the reflectance correction factor for each pixel derived from the radiometric calibration that is specific for the reflectance plate used. From visual inspection, images with a clear saturation of the 10-bit range were not used for calibration data.

As the shutter speed and ISO settings of the camera affects the DN values within the image several radiometric calibration runs were made with different settings. The argument stems from the fact that the calibration coefficient, as seen in equation 3, which is derived from the radiometric calibration depends on the settings of the camera. For example, if the radiometric calibration is done with a specific ISO and shutter speed while the actual flight is done with other settings the calibration coefficient can produce errors of estimated reflectance. Hence, three radiometric calibrations were done using a 99% and 50% spectralon reflectance plate (Labsphere inc., New Hampshire, USA). The first was done with automatic shutter speed and ISO using the 99% spectralon reflectance plate for the downward looking sensor (V_{2obs}).

The other two radiometric calibration were done with manual shutter speed and ISO with a 99% and 50% spectralon reflectance plate for the downward looking sensor (V_{2obs}). The spectral reflectance curve for the 99% reflectance plate is uniform across the wavelengths according to the provided metadata from the manufacturer – leaving the R_L at a value of 0.99 for all the individual sensors. The spectral reflectance of the 50% reflectance plate is not uniform across the spectrum according to the manufacturer provided metadata. Thus, an approximation was made for the 50% reflectance plate. The central wavelength for the individual sensors governed which reflectance value was used for R_L in equation 4 as can be seen in table 1. Hence, the spectral sensitivity of the individual sensors was assumed to be uniform within their bandwidth. If the spectral sensitivity is not assumed uniform within the bandwidth of the sensor the R_L used would have to be weighted towards the part of the bandwidth with the largest sensitivity.

Table 1: Values of R_L used for the four individual sensors during the manual radiometric calibration run using the 50% reflectance plate. The central wavelength of the individual sensors was used to derive the value provided by the manufacturer.

Sensor	R_L value used
Green	0.4992
Red	0.5167
NIR	0.5358
REG	0.5281

The Parrot Sequoia was set to capture an image and thus also a corresponding sunshine sensor reading at a 1.5 second interval for all the radiometric calibrations regardless of settings as it was the shortest interval possible to choose. As the sunshine sensor reads incoming light 9 times prior to each image and thus the mean value was chosen as the final sunshine reading for the image in question. The radiometric calibration runs were done on the roof of the Department of Physical Geography and Ecosystems Science at Lund University.

4.2.1   Radiometric calibration with automatic settings

The radiometric calibration with automatic settings on the camera implies the camera choosing what is deemed optimal settings for an image taken at that moment. The ISO number was constant at 100 for all sensors during the calibration. The radiometric calibration run with automatic settings were done during mostly cloudy conditions at solar noon for 96 minutes. The setting that was most dynamic was the shutter speed as can be seen in table 1.

Table 2: Exposure used by the camera during the automatic settings radiometric calibration. In this calibration run the camera set its exposure/shutter speed automatically.

Sensor	Shutter speed in microseconds (µs)	Note
Green	184 – 207 µs	Mostly uniform at 184
NIR	184 – 1592 µs	Mostly uniform at 184
RED	184 – 507 µs	Mostly uniform at 184
REG	392 – 2999 µs	Non-uniform within the range

4.2.2   Radiometric calibration with manual settings

The second and third radiometric calibration were done with static manual settings. These settings were derived from analysing images taken in field with various vegetation covers to see what ISO number and shutter speed that was typically used by the camera. The ISO number was constant for all the images taken in the field. The shutter speed varied with illumination conditions and was overall shorter during clear conditions and longer during cloudy conditions. During the radiometric calibration it was noted that the camera was unable to take pictures at specific shutter speeds during a run. However, a decrease of the shutter speed for the different sensors resulted in the camera being able to take pictures. Hence, the original manual settings derived could not be used and had to be reduced by half. The problem probably stems from the fact that the camera is not being able to fully compensate for differences in illumination intensities. Consequently, the camera did not take a picture if illumination conditions were too bright for the corresponding shutter speed – protecting the sensors. However, this is not confirmed by the manufacturer. Hence, the reduced shutter speeds resulted in the camera being able to fulfil one 30 and one 45-minute run for the 50% and 99% reflectance plates respectively. Both runs were done during cloudy conditions during solar noon to decrease shifts in illumination intensity due to sun angles. The weather thus controlled how long the runs were able to last. The final shutter speed values chosen can be seen in table 3.

Table 3: Shows the exposure/shutter speed chosen to be used for the manual settings radiometric calibration to be used with flights. The values were derived from analysing taken images in the field at various locations with various illumination conditions.

Sensor	Exposure/shutter speed in microseconds (µs)
Green	400 µs
NIR	200 µs
RED	400 µs
REG	800 µs

4.3   Sunshine sensor performance

The sunshine sensor performance was tested with the automatic settings radiometric calibration run by simultaneous measurements with factory calibrated multispectral sensors (Skye instruments ltd. Model 48671, Powys, U.K). Two of the wavelength bands present in the Skye sensors overlapped those in the Parrot Sequoia making it possible to compare the performance of those Parrot Sequoia sunshine sensor channels. The Skye sensor channels that were compared were channel 1 at 647-667nm and channel 3 at 733-743. It should be noted, however, that the spectral ranges do not overlap perfectly.

The Skye sensor facing upwards made readings at a 2 second intervals compared to the 1.5 seconds of the Parrot Sequoia. This implied that both sensors timeseries readings had to be resampled and interpolated to a 1 second interval with offset correction to be able to correlate the sensor readings to each other. The offset correction was applied to the Parrot Sequoia time series so that the first measurement coincided at an exact second resulting in 39 milliseconds offset. The resampling and interpolation was done using the Pandas module in the Python programming language with a linear interpolation function. The gain channel of sunshine sensor for all bands during the whole run was 1.

4.4   Noise correction

Dark offset images were created so that the impact of the camera electronics on the sensor could be quantified and used for rectification. The rectification of dark current was done according the method described in Kelcey & Lucieer (2012) as a dark offset subtraction on a pixel-by-pixel basis. The test to obtain dark offset images to determine the noise was done in a dark room with dark cloth covering the lenses with an image taken every 1.5 second for a total of 35 minutes to let the camera get warm and stabilize. Furthermore, the long timespan of the test made it possible to analyse how noise increased with temperature. The mean value of DN of an image is highly sensitive to random noise, as in certain pixels with high values. This means that the median is less sensitive to these certain outliers thus the median was used to define the systematic noise present in an image.

It should be noted that the dark offset run was done with automatic settings on the camera. This was due to the camera not taking images with manual settings. This is probably due to the camera not being able to detect any distinct radiation signal thus not taking an image. Hence, a dark offset curve could not be made with manual settings. Thus, an approximation was made to use the Parrot Sequoias own dark offset measurement as the basis for the dark offset correction. The dark offset measurement is stored as EXIF/XMP information. The random noise of the sensors was not rectified in this study.

A dark current offset was done for the sunshine sensor. However, there was no noise present in the sunshine sensor, so no dark offset subtraction was needed. Information about sunshine temperature was not analysed due to the camera not storing sunshine sensor temperature information in EXIF/XMP form.

Descriptive statistics as mean and median values were calculated for the dark current runs to discern between noise of outlies and systematic background noise respectively.

4.5 Vignetting correction

To test the amount of vignetting within an image the images taken during the radiometric calibration were analysed. This was done since for asses vignetting it is necessary for the image to be taken at a Lambertian surface and under homogenous illumination conditions (Bachmann et al., 2013). These conditions were satisfied during the manual settings radiometric calibration runs with the 50% reflectance plate. Statistics on the vignetting were produced by stacking all images taken and calculating the mean pixel to determine the average vignetting during the calibration run.

The radiometric calibration equation used in this study (Eq. 5) derives a reflectance correction factor for every pixel. This implies that the equation enables a flatfield correction if a geometrically and radiometrically uniform surface is used to radiometrically calibrate the camera. This is the case with the Spectralon reflectance plates used in this experiment which is flat and has a uniform reflectance across the surface. Thus, pre-processing and rectification of vignetting is deemed redundant. For example, if the DN values were to decrease radially from the image centre it would imply that the reflectance correction factor increases radially as well – thus compensating for the vignetting on a pixel-by-pixel basis. If a single reflectance factor was to be used for all the pixels and not being pixel unique then vignetting would have to be corrected for in a pre-processing manner.

4.6 Field testing of the radiometric calibration

To test the performance of the radiometric calibration, dark current correction and vignetting in real world conditions, flight tests were conducted. A flight was done at Lönnstorp experimental crop plots, maintained and run by SLU (Swedish Agricultural University), outside of Lund. Illumination conditions during field testing were clear skies at solar noon. The UAV used was a 3DR Solo (3DR Robotics Inc, Berkley, USA) with the Parrot Sequoia camera and sunshine sensor mounted.

The performance of the corrections was tested by taking images at 10 and 60 meters height of four Spectralon reflectance panels placed upon a dark green tarp (Labsphere inc., USA). This was done to test how well the given reflectance of the panels could be replicated by the camera after radiometric calibration by the radiometric calibration data. Reflectance panels used for validation were at 5, 20,

50 and 99% reflectance with a non-uniform reflectance depending on wavelength, apart from the 99% panel. The central wavelength for the different camera sensors was used to choose the spectral reflectance of the plates hence assuming that the spectral sensitivity is uniform.

In addition, NDVI measurements were taken at two plots, 3x3 meters, in separate fields with a handheld NDVI spectrometer (Skye instruments ltd., U.K) at a height of 1 meter with central wavebands at 650nm and 860nm for the red and NIR band respectively. The handheld NVDI spectrometer measures the outgoing radiation in a 50-degree cone thus the signal received is in parts the mean of the plot. The UAV derived mean NDVI in the plots were calculated using the corrected and radiometric calibrated images from the Parrot Sequoia. For further comparison NDVI were also calculated for the plots using non-corrected and non-radiometric calibrated images from the Parrot Sequoia.

5   Results

In this section the results of the various tests are presented. Results include the performance of the sunshine sensor, dark current tests, vignetting. Furthermore, the performance of the different radiometric calibrations on field acquired images are presented. All results are visualized with figures using the Python programming language. Data and code used is free of access upon asking (Contact me: Karl.Adler92@gmail.com).

5.1   Sunshine sensor performance results

The Parrot Sequoia sunshine sensor and Skye sensor both show a similar behaviour of responsiveness to incoming radiation in the red wavelength band (figure 1). Furthermore, the Parrot Sequoia in the Red band possess a large range of DN values ranging from circa 300 to 1800.
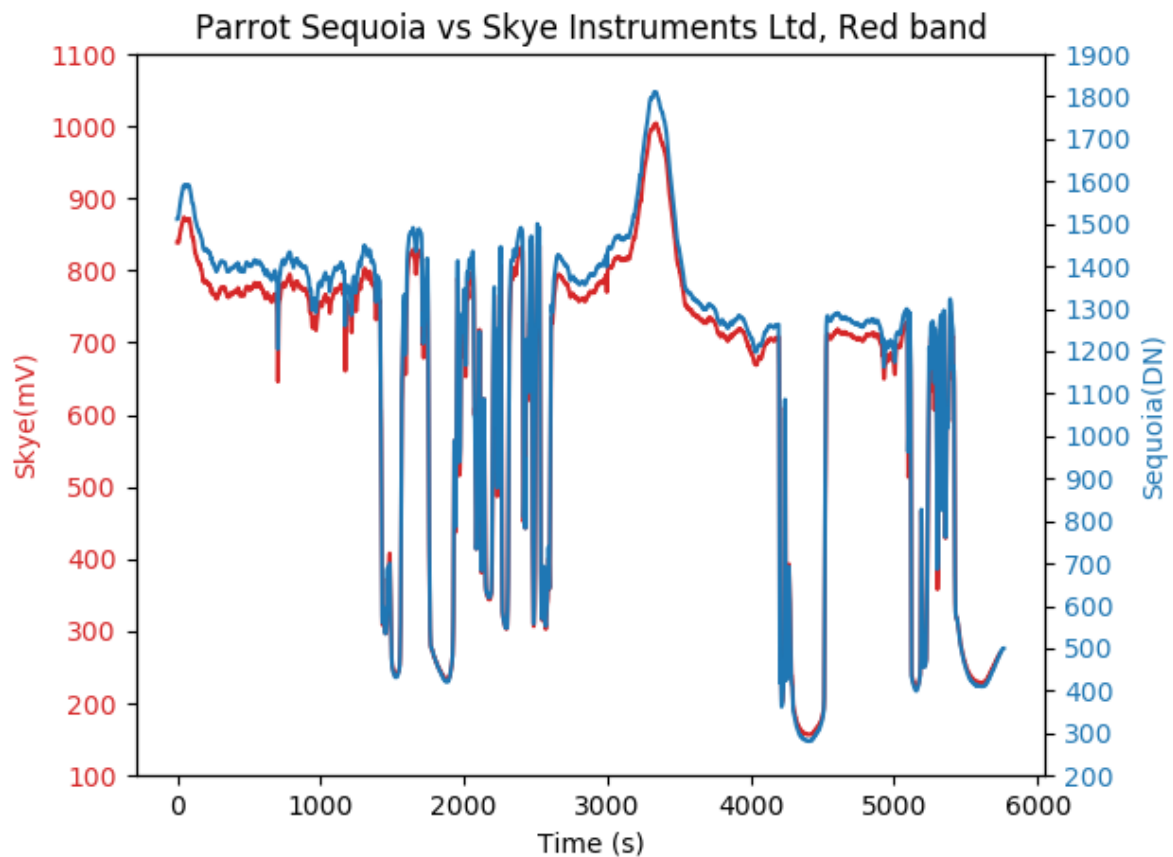

Figure 1: Plot showing the resampled and interpolated Skye instruments ltd channel 1 facing upwards (mv) vs the Parrot Sequoia sunshine sensor Red band (DN). The parrot Sequoia recorded at n 1.5 second interval while the Skye Instruments ltd at a 2 second interval. Both data sets were resampled to 1 second intervals with a linear interpolation.

The Parrot Sequoia sunshine sensor and Skye sensor both show a similar behaviour of responsiveness to incoming radiation in the REG wavelength band (figure 2). This responsiveness is similar to what could be observed for the red wavelength band as presented in figure 1. However, the total range of DN values for the Parrot Sequoia in the REG band ranges from circa 50 to 500. This range is smaller compared to the Red band for the sunshine sensor.
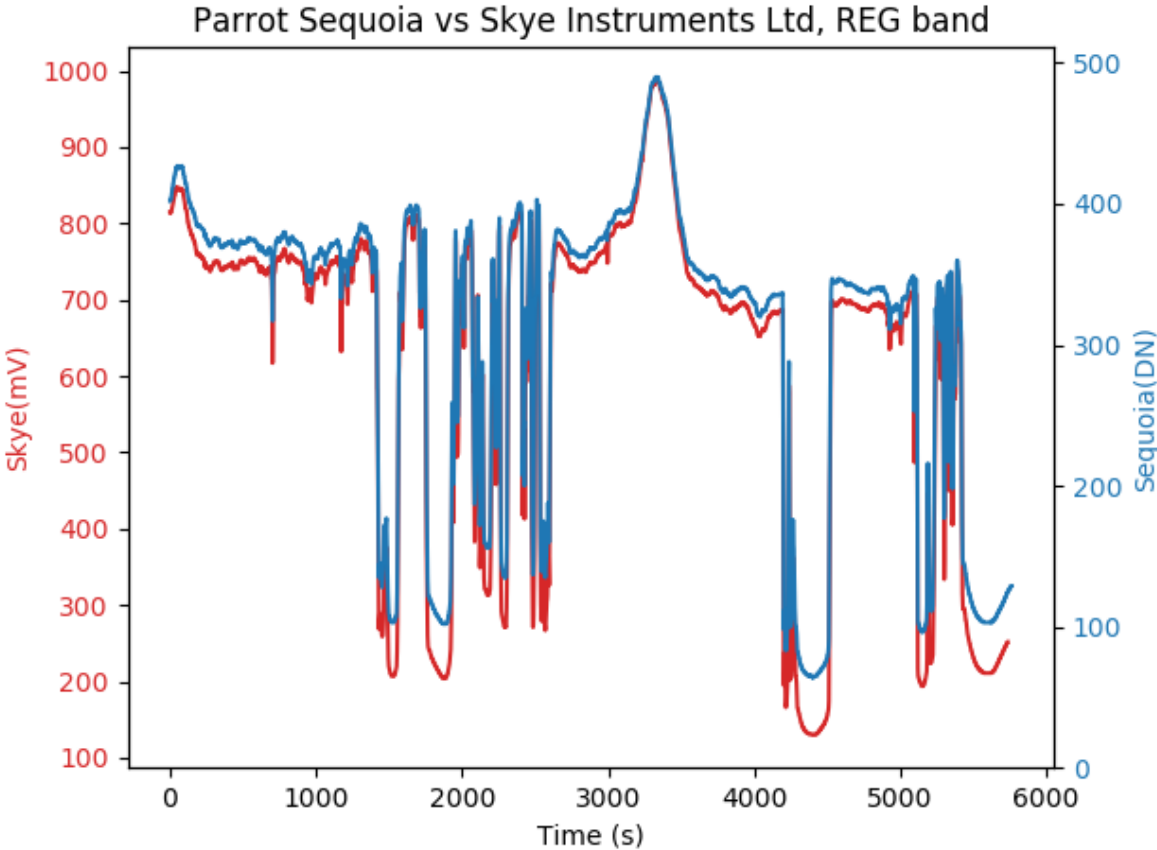

Figure 2: Plot showing the resampled and interpolated Skye instruments ltd channel 3 facing upwards (mV) vs the Parrot Sequoia sunshine sensor REG band (DN). The parrot Sequoia recorded at n 1.5 second interval while the Skye Instruments ltd at a 2 second interval. Both data sets were resampled to 1 second intervals with a linear interpolation.

5.2   Dark current test results

The Parrot Sequoia's 4 different camera sensors show identical behaviour in temperature response when utilizing automatic camera settings during the dark offset experiment (Figure 3). The temperature increases in a rapid fashion during the dark current run with a sharp increase of temperature in a short amount of time.
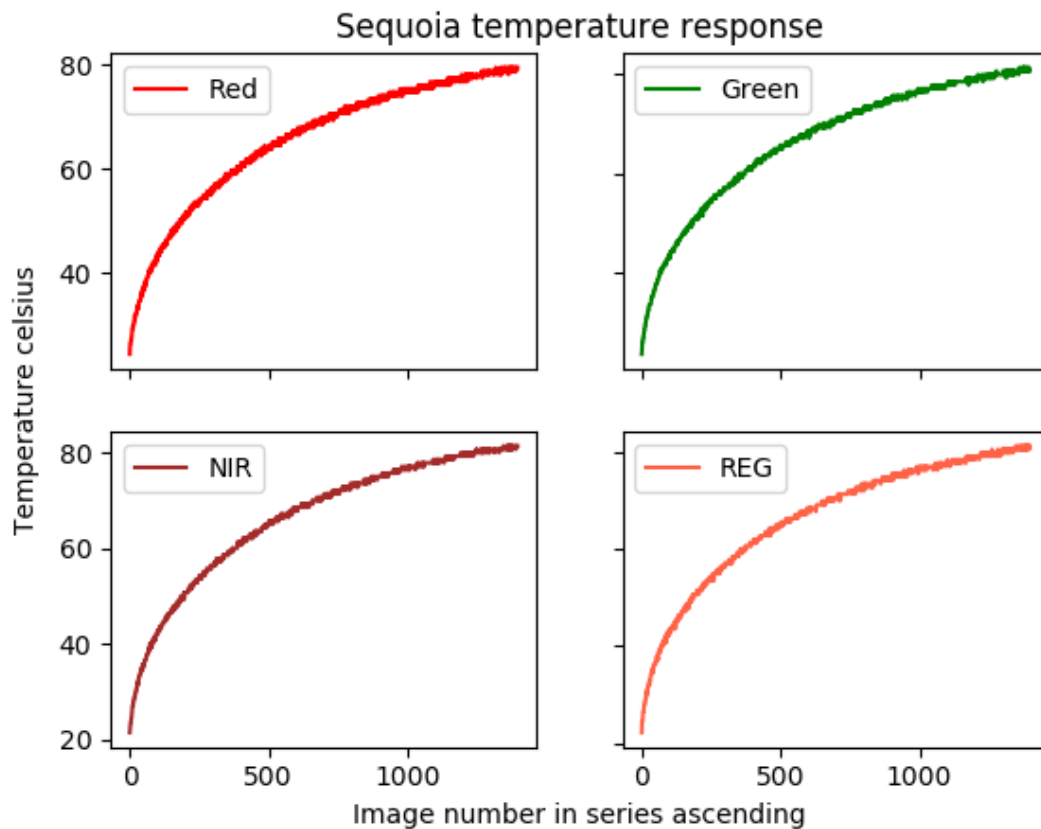

Figure 3: Plot showing the temperature response of the four individual bands in the Parrot Sequoia camera for a 35-minute dark current test with automatic camera settings. The y-axis represent temperature is Celsius. The y-axis represents image number in order during the 35-minute dark current testing i.e. 0 is the first image taken in the run. Images were taken at 1.5 second intervals.

During real-world testing the camera, depending on weather conditions, temperatures normally varies around 30-50 degrees Celsius. For instance, for images taken last summer at Abisko, in the north of Sweden, the temperature varied between 40-50 degrees Celsius. During radiometric calibration in early spring in southern Sweden the camera temperature was around 30-40 degrees Celsius.

Mean image pixel value in relation to temperature during the dark current experiment show an identical behaviour for all the bands (Figure 4). At First there is a drastic increase in mean image pixel value up to 50-60 degrees Celsius, thereafter the rate reduces and stabilizes at a mean image pixel value at around 150 for all the bands.
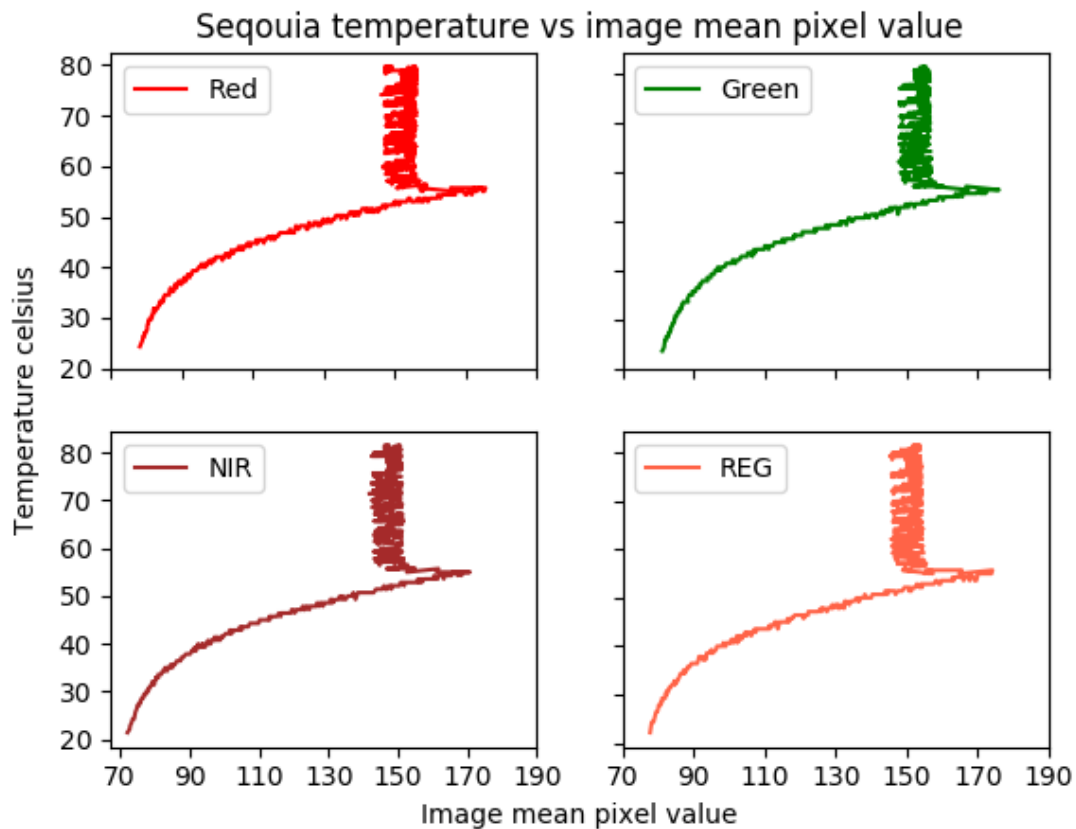

Figure 4: Plot showing the temperature versus the image mean pixel value for the Parrot Sequoia four individual camera sensors for a 35-minute dark current test with automatic camera settings. The x-axis represents the image mean pixel value i.e. the mean value from the whole image. The y-axis represents the temperature in Celsius. Recordings were done at a 1.5 second interval.

The shutter speed was constant throughout the dark current run at 3000µs. The ISO was constant at 6375 until the 55 degrees Celsius mark. However, when the camera reached 55 degrees Celsius the ISO number started to decrease. At the last recoding the ISO number was 1050. Hence, the ISO number decrease could be an explanation to for the decrease in image mean value. The median pixel value for an image at the start and end of the dark current test is shown in table 4.

When comparing the image median values (table 3) to the image mean values (figure 4) it can be noted that the image median value is less affected by temperature changes. The four bands behave differently as can be seen in table 3 where median of the NIR band image is stagnant from start to end while the Red increases from 67 to 79 for instance. During the test the cameras internally logged dark current value, encoded within every image, was static at 75 for all the bands. This logged dark current value is thus incorrect, but closer to the image median pixel value than the mean image pixel value.

Table 4: Table showing the median pixel value for the first and last image for the dark current test for the four separate camera bands in the Parrot Sequoia.

	Image median at start of dark current test	Image median at the end of dark current test	% Change in median
Green	77	81	+ 5.1%
Red	67	79	+ 17.9%
NIR	73	73	0%
REG	73	83	+ 13.6%

The overall noise present within an image increases drastically with increased temperature (figure 5). This behaviour is prevalent for all the bands where at low temperatures the noise within an image is low whereas with increased temperatures the noise is increased. The first image taken in the green band, to the left in figure 5, was at a temperature of 23.5 degrees Celsius were as image number 1937 taken, to the right in figure 5, was at a temperature of 80.7 degrees Celsius.
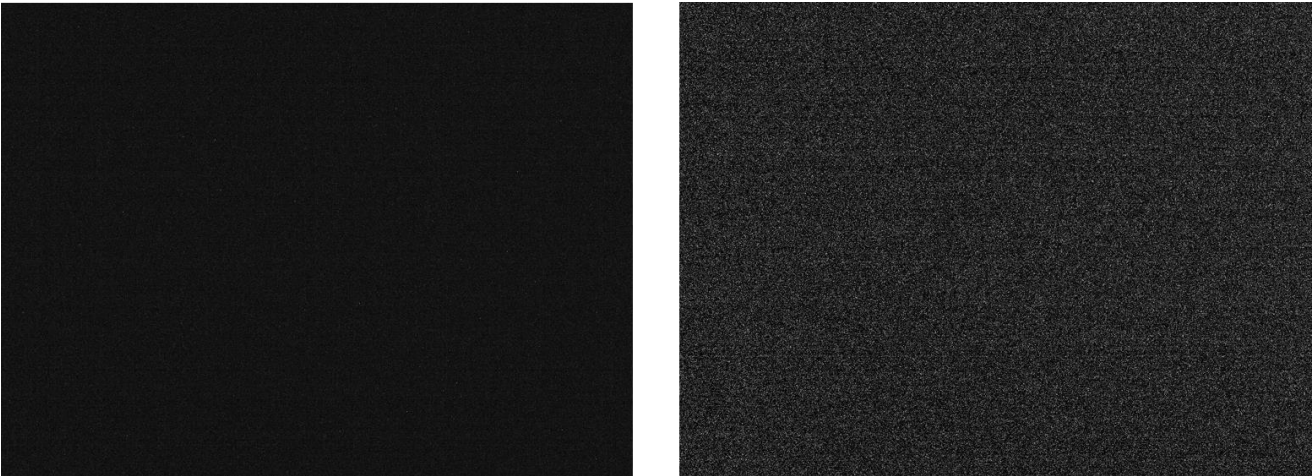

Figure 5: First and last image taken during the dark current test for the green band in the Parrot Sequoia camera. To the left is the first image taken and to the right is image 1397 – the last image.

5.3 Vignetting test

The vignetting effect for the green, red and NIR sensors show overall similar behaviour where the REG band stands apart (Figure 6). It should be noted that the vignetting shape is similar but the range of values is different for the separate bands. The vignetting was calculated by stacking all images for each band to get the mean value of every pixel. This made it possible to determine the mean vignetting for the three horizontal transects to be quantified. For all the separate bands the vignetting is similar in the top, middle and bottom of the image.
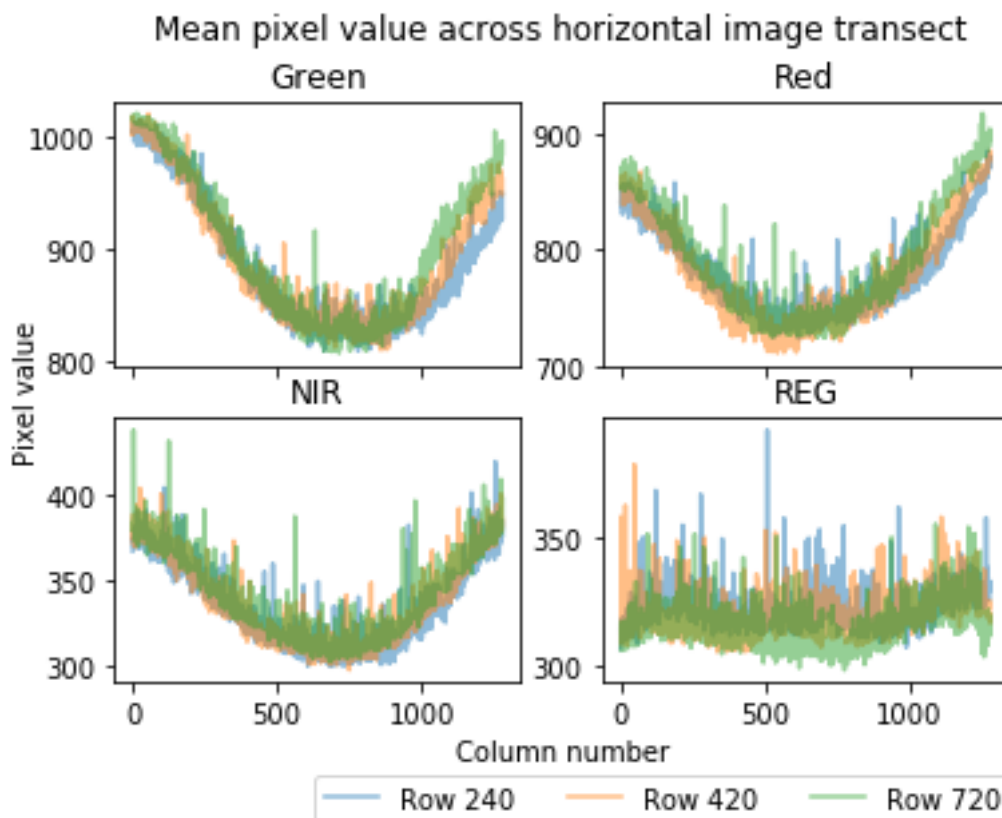

Figure 6: Showing the mean pixel value across three horizontal line transects at row 240, 420 and 720 for the four individual sensors. The mean value for every pixel across the transect is derived from 1131 images gathered during radiometric calibration using a 50% Spectralon reflectance plate. It should be noted that the y-axis has different ranges for the separate bands.

The vignetting effect is more prevalent for the green and red band. However, the REG band shows a different, more erratic, behaviour with no distinct vignetting. In the Green and Red band, the outermost edges in the images are close to saturate the 10-bit range (0-1024). Furthermore, the vignetting is not symmetrical across the image depending on the sensor in question. For instance, the green band exhibits larger values to the left side of the image compared to the right, while the opposite is seen in the REG band. It can further be seen that various noise is present across the transects, with the REG band exhibiting more noise than the other bands. The vignetting seen is not a radial decrease in values but rather an outward increase in values in a non-radial shape (Figure 7).

21

Figure 7: An image taken of a 50% Spectralon reflectance panel during the manual radiometric calibration in the Green band where vignetting can be seen. The image taken is part of the dataset used to derive the vignetting statistics. The image taken was done during radiometric calibration using a 50% spectralon reflectance plate. The green band was chosen as of visualization purposes.

5.4 Calibration performance

The calibration data derived from the 50% reflectance plate can recreate the target reflectance of the 50% reflectance plate in NIR and REG (Figure 8). However, the green and red bands show this reversed vignetting with higher values towards the edges of the images. This means that the radiometric calibration in this case did solve the vignetting problem for the NIR and REG band but not the green and red band. The NIR and REG band show no signs of vignetting and banding but have more pronounced random noise. The NIR band, as shown previously in figure 6, does exhibit vignetting that is rectified by the radiometric calibration.
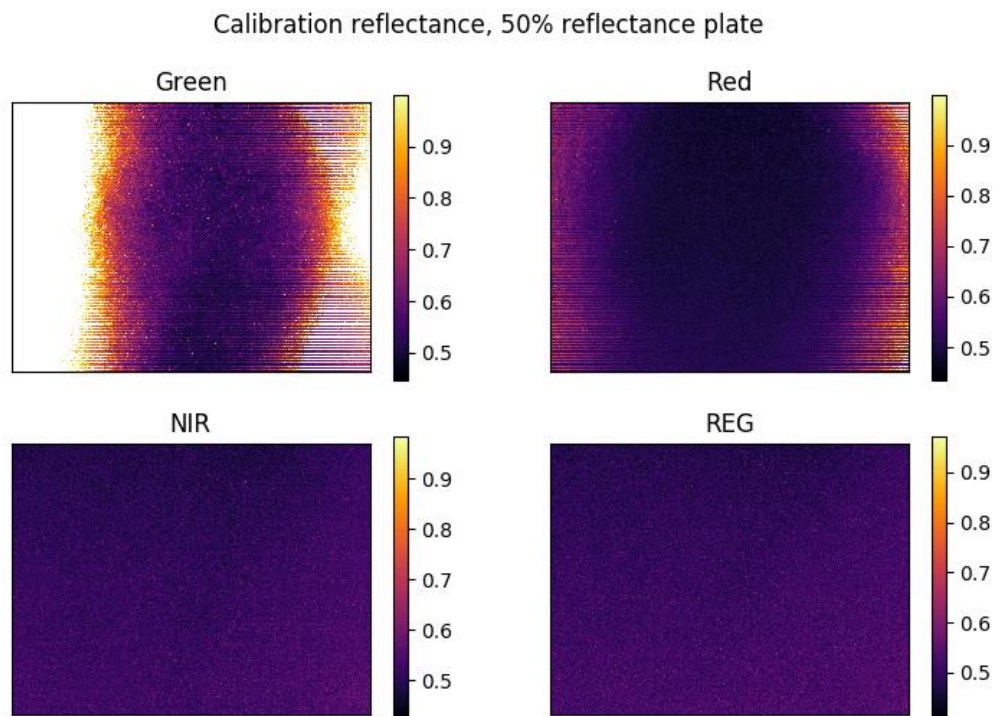

Figure 8: Images with applied radiometric calibration produced from the 50% reflectance plate calibration data upon a randomly selected image within that dataset. Reflectance is expressed in decimal form. White areas correspond to pixels having reflectance values exceeding 1 or being below 0.

Apart from the vignetting seen there is also some horizontal banding present in the green and red band represented as varying lines of lower and higher values of estimated reflectance. Pixels with estimated reflectance values outside of the possible range of reflectance values (0 to 1) were omitted. The number of pixels omitted due to being outside of the possible reflectance range are 30% (green), 2% (red), 0% (NIR) and 0% (REG). The descriptive statistics of the images can be seen in table 5 together with descriptive statistics of images.

The mean and median reflectance for the wavebands, apart from the green band, are close to the target reflectance. The green band shows a higher reflectance of more than 10% compared to the

other bands which are below or above 3% of the target reflectance. The closeness of the median and the mean present in all the bands, except the green band, implies a non-skewed distribution of reflectance values in the images.

Table 5: Showing the descriptive statistics of the images presented in figure 8. The target reflectance corresponds to the manufacturer given reflectance in the given waveband which is the reflectance value trying to be modelled. Pixels in the image having a reflectance value above 1 or below 0 were omitted.

	Mean	Median	Min	Max	Standard deviation	Target reflectance
Green	0.636	0.59	0.448	1	0.124	0.499
Red	0.53	0.511	0.436	1	0.074	0.517
NIR	0.517	0.516	0.419	0.983	0.026	0.535
REG	0.506	0.505	0.402	0.971	0.0.26	0.528

The relationship between the pixels and the sunshine sensor show varying degrees of linearity from edge to centre in the green band (Figure 9). The pixel at the left side of the image in the green band show severe saturation of the 10-bit range for the pixel resulting in a skewed relationship (Left image in figure 9). The pixel in the centre of the image show less of this saturation compared to the pixel at the left, resulting in a more linear relationship (Right image in figure 9). However, there is still some saturation present of pixel values at the central pixel. The skewed relationship seen at the left pixel, that exhibits severe saturation, coincides with the area within the green band that had non-accurate estimations of reflectance (Figure 8). The less skewed relationship seen in the central pixel, that exhibits less saturation, coincides with the area present within the green band that was able to produce sensible estimations of reflectance (Figure 8).
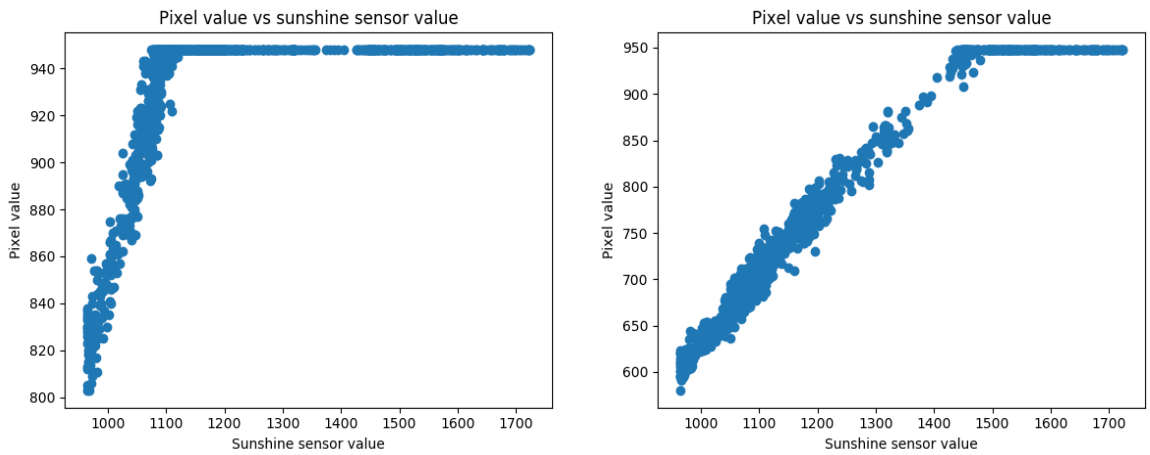

Figure 9: Two scatterplots showing the relationship between pixel value and sunshine sensor values measured during the 50% calibration run for two pixels in the green band. To the left is the pixel at row 480 and column 1, central left edge of the image. To the right is the pixel at row 480 and column 640, centre of image.

The *K* factor used to produce the reflectance correction matrix using the 50% reflectance plate show a different distribution of values with different band (Figure 10). The distribution of *K* values for the bands show a close similarity to the distribution seen of estimated reflectance values presented in figure 8.
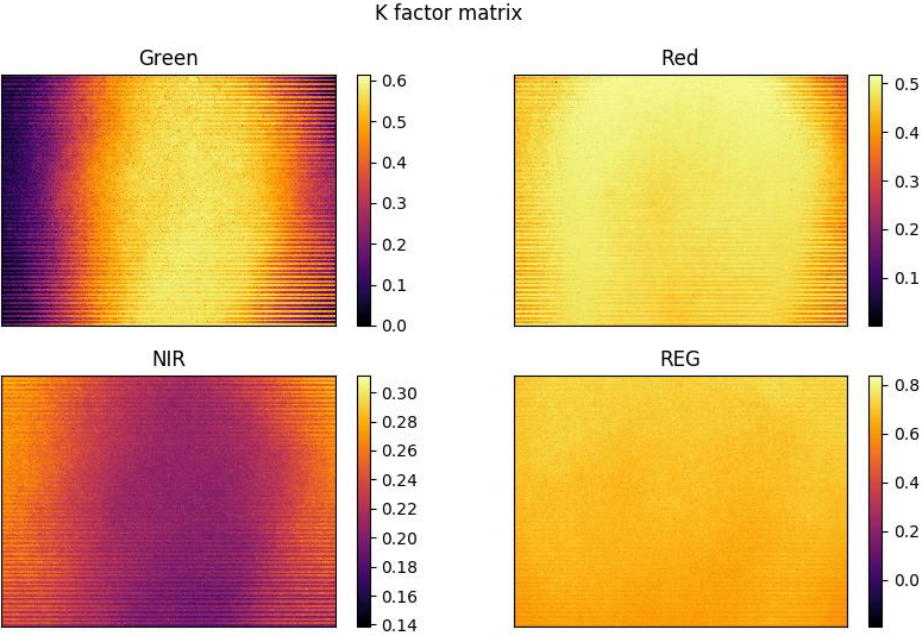

Figure 10: Images representing the K factor matrix used for the reflectance correction matrix produced from the radiometric calibration data run using the 50% reflectance plate.

The calibration data derived from the radiometric calibration run using the 99% plate show severe saturation (Figure 11). This resulted in many pixels being omitted due to having estimated reflectance values above or below the possible range of reflectance values (0 to 1). As with the 50% calibration data the vignetting is still present for the green band but not for the red band. The NIR and REG band show some vignetting towards the right edge.

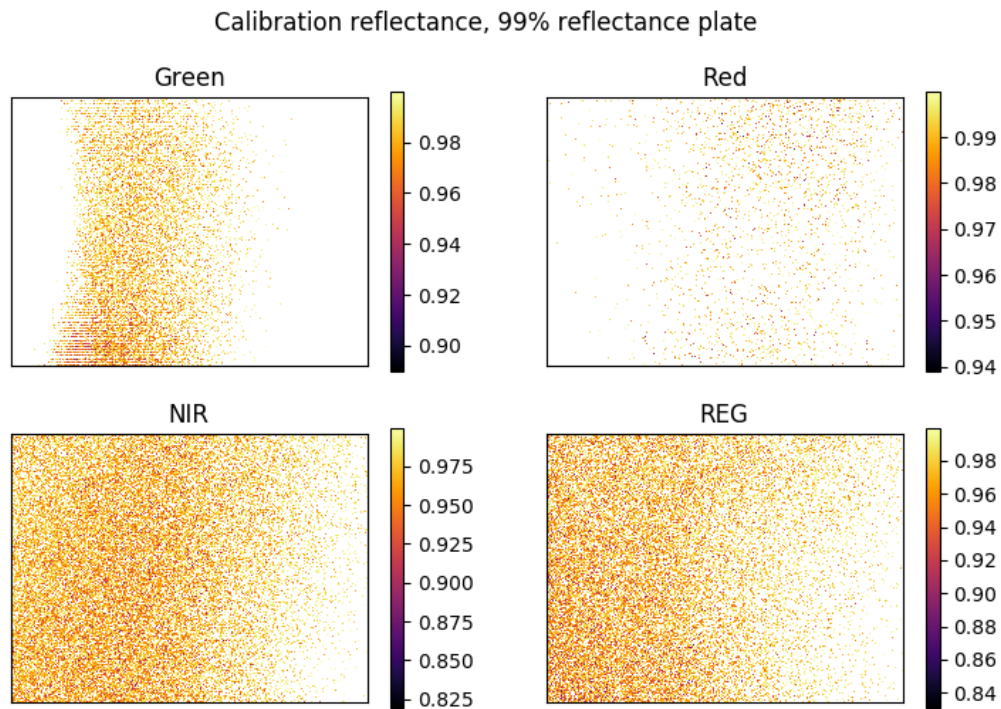Calibration reflectance, 99% reflectance plate

Figure 11: The calibration data produced from the 99% reflectance plate upon a randomly selected image within that dataset. Reflectance is expressed in decimal form. White areas correspond to pixels having values exceeding 1 or being below 0.

The number of omitted pixels for the 99% calibration run was 81% (Green), 94% (Red), 49% (NIR) and 58% (REG). The number of pixels that were outside of the possible reflectance range is significantly higher compared to the 50% calibration data. The descriptive statistics of the images presented in figure 9 can be seen in table 6. The pixels that were not omitted show that the mean and median reflectance is close to the target reflectance of 99% (Table 6). However, the high omission of pixels indicates that the 99% radiometric calibration data is not able to estimate the 99% reflectance plate. This implies that the results cannot be trusted and thus the 99% radiometric calibration data was not applied upon the field images.

Table 6: Showing the descriptive statistics of the images presented in figure 8. The target reflectance corresponds to the manufacturer given reflectance in the given waveband which is the reflectance value trying to be modelled. Pixels in the image with reflectance values over 1 or below 0 were omitted.

	Mean	Median	Min	Max	Standard deviation	Target reflectance
Green	0.982	0.985	0.89	1	0.013	0.99
Red	0.991	0.993	0.939	1	0.007	0.99
NIR	0.968	0.971	0.819	1	0.022	0.99
REG	0.969	0.973	0.831	1	0.022	0.99

The radiometric calibration data derived from the automatic calibration run provided no meaningful reflectance data for any of the bands except the green band, but with only 10% of the pixels being within the possible reflectance range. For example, the automatic calibration applied upon the red band returned no pixels within the possible reflectance range and reflectance values in several bands being far below or above the possible range of reflectance. Hence, the result showing the automatic calibration performance at reproducing the 99% reflectance plate used would only show images with no pixels within the possible range of reflectance values. Thus, the automatic calibration data was not applied on the field images.

5.5   Field testing of reflectance and NDVI

In this section images taken during the field campaign is presented with the 50% reflectance plate calibration data applied on images taken at 10 and 60 meters height. For all the images, the area of the image containing the tarp with the Spectralon reflectance plates upon it are cropped out for better visualization. The tarp with the reflectance plates upon was at the centre of every image.

The reflectance produced with the 50% calibration data at a height of 10 meters show varying results depending on waveband (Figure 12). The green and red band cannot reproduce the reflectance of the 50 and 99% reflectance plates (Table 7). However, the lower reflectance plates of 5 and 20% are closer to the target reflectance for each band (Table 7). The NIR and REG are very close at reproducing the reflectance of the different plates but in the end fall short at reproducing the 99% reflectance plate with a under estimation of reflectance (Figure 12).

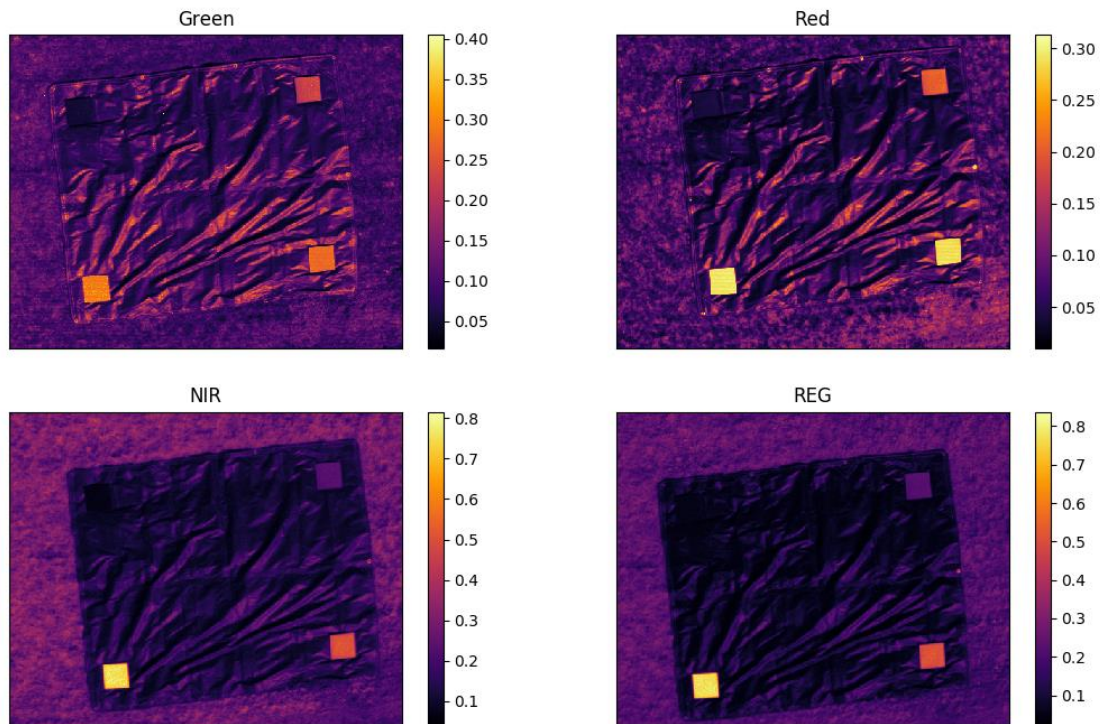Field reflectance - 10m height, 50% reflectance plate calibration

Figure 12: The reflectance of four reflectance plates for each band at a capture height of 10 meters using the 50% reflectance plate calibration data. The four reflectance plates lie on a tarp where the top left is a 5% plate, top right a 20% plate, bottom right a 50% plate and bottom left a 99% plate. The images are cropped to only include the tarp with the tarp being in the centre of the original image.

At a height of 60 meters the 50% calibration data produces generally lower reflectance values for each band (Figure 13). Still the green and red band cannot reproduce the target reflectance of the 50 and 99% reflectance plates (Table 7). The REG band show similar performance compared to a capture height of 10 meters but with a greater under estimation of reflectance values overall (Table 7). The NIR band show over estimation of target reflectance for the different reflectance plates with the 50% reflectance plate being the clearest indicator (Figure 13)
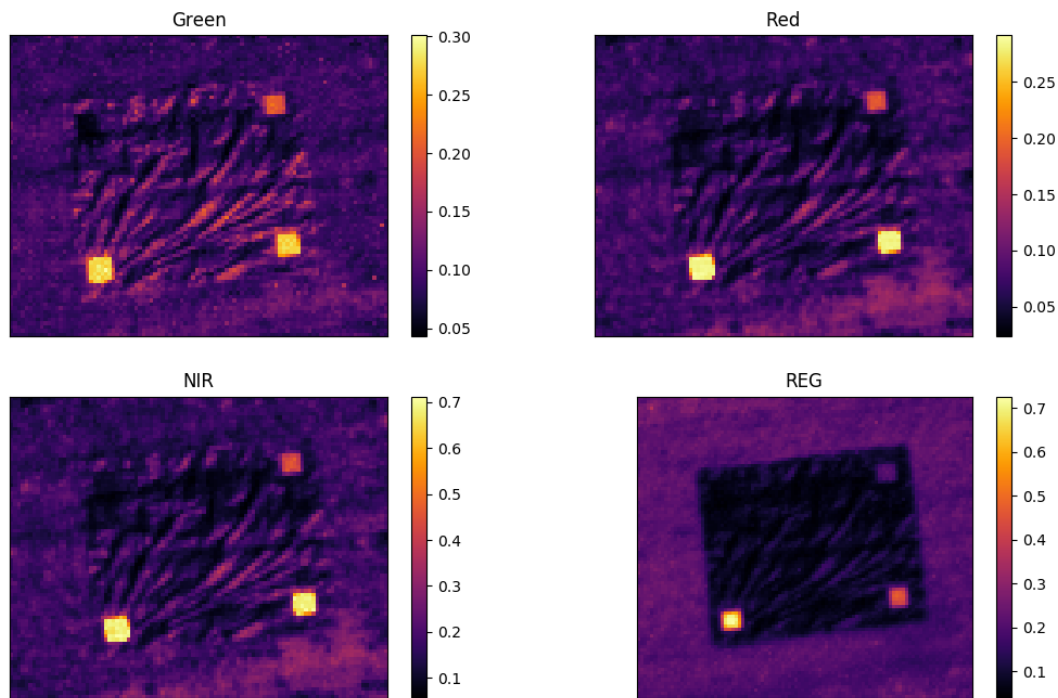
Figure 13: The reflectance of four reflectance plates for each band at a capture height of 60 meters using the 50% reflectance plate calibration data. The four reflectance plates lie on a tarp where the top left is a 5% plate, top right a 20% plate, bottom right a 50% plate and bottom left a 99% plate. The images are cropped to only include the tarp with the tarp being in the centre of the original image.

The mean reflectance for each plate with the different configurations of calibration data and capture height show varying accuracies (Table 7). For instance, the mean predicted reflectance of the 5% reflectance plate in the green band using the 50% radiometric calibration data is 0.052 while according to the manufacturer of the plate the reflectance in that wavelength should be 0.037 – showing an under estimation of reflectance of 40%. The mean reflectance for the 5 and 20% show no distinct changes regardless of capture height with an error of 40%. The mean reflectance of the 20% reflectance plate shows the smallest error in target reflectance. However, as noted previously the mean reflectance for the 50 and 99% is far below the target reflectance regardless of calibration data and capture height used with an error around 70%.

The red band show different behaviour compared to the green band with drastically smaller error of estimated mean reflectance for the 5% reflectance panel (Table 7). The estimated reflectance of the 20% reflectance panel is much higher at a capture height of 60 meters compared to 10 meters in the red band. As with the green band the red band still under estimates the reflectance of the 50 and 99% reflectance plates with a similar error.

The NIR band shows high amounts of error in estimated mean reflectance of the 5% reflectance plate at a capture height of 10 meters (Table 7). The estimated reflectance of the 20 and 50% reflectance plates show low error under the 5% mark. However, with a capture height of 60 meters the estimated mean reflectance for all the plates are generally doubled compared to the capture flight of 10 meters. This means that there is an over estimation of reflectance for the 5, 20 and 50% reflectance plates compared to the target reflectance. The cause of this increase at this height is unknown and could be the product of a sudden burst of incoming solar radiation. However, even with this over estimation there is still an under estimation of the 99% reflectance plate.

The REG band compared to the NIR band show a similar error in estimated mean reflectance regardless of capture height (Table 7). The estimated mean reflectance for the 5% reflectance plate is on par with the green band with an error around the 40% mark. As with all the other bands there is still an under estimation of the 99% reflectance plate even if the error is the smallest compared to the other bands.

Table 7: Showing the mean reflectance for each plate present in the field images for the different calibration data and capture height. Reflectance is expressed in decimal form where each plate has a target reflectance acquired from the manufacturer data from each spectralon reflectance plate. I.e. column two corresponds to the calibration data acquired with the 50% reflectance plate at a capture height of 10 meters. The target reflectance is derived from assuming the spectral sensitivity within the band is uniform. * = error compared to the target reflectance in %. The calculated error is rounded to the closest integer.

	Reflectance plate	Predicted mean reflectance, 50% calibration at 10 meters	Predicted mean reflectance, 50% calibration at 60 meters	Actual plate reflectance
Green	5%	0.052 *(40%)**	0.052 *(40%)**	0.037
	20%	0.225 *(6%)**	0.203 *(4%)**	0.212
	50%	0.275 *(44%)**	0.273 *(45%)**	0.499
	99%	0.295 *(70%)**	0.279 *(71%)**	0.99
Red	5%	0.042 *(7%)**	0.045 *(15%)**	0.039
	20%	0.202 *(9%)**	0.177 *(20%)**	0.224
	50%	0.288 *(44%)**	0.278 *(46%)**	0.516
	99%	0.293 *(70%)**	0.282 *(71%)**	0.99
NIR	5%	0.07 *(70%)**	0.105 *(150%)**	0.041
	20%	0.234 *(1%)**	0.437 *(83%)**	0.238
	50%	0.508 *(5%)**	0.682 *(27%)**	0.535
	99%	0.755 *(23%)**	0.688 *(30%)**	0.99
REG	5%	0.054 *(35%)**	0.059 *(47%)**	0.04
	20%	0.221 *(5%)**	0.228 *(2%)**	0.232
	50%	0.511 *(3%)**	0.495 *(6%)**	0.528
	99%	0.777 *(22%)**	0.766 *(23%)**	0.99

5.5.1 Field NDVI

The NDVI values calculated from the handheld spectrometer and the calibrated Sequoia data deviate by 0.017 and 0.019 in plot 1 and 2 respectively (Table 8). In plot 1 the calibrated Sequoia data equals a slightly higher NDVI compared to the handheld spectrometer while for plot 2 it is the opposite. However, the un-calibrated Sequoia data show a drastically lower NDVI compared to the handheld spectrometer and calibrated Sequoia data. This means that a radiometric correction will produce a higher NDVI compared to no radiometric correction. Furthermore, it should be noted that the median calculated NDVI from calibrated data were 0.704 and 0.58 for plot 1 and plot 2 respectively. This implies that the distribution of NDVI values within the plots are not to skewed as they correspond quite close to the mean.

Table 8: The NDVI calculated for the two plots on separate cropping fields using a handheld spectrometer, un-calibrated Sequoia data, Sequoia data calibrated with the 50% reflectance plate calibration data. The NDVI calculated is the mean for the whole plot.

	Plot 1 mean NDVI	Plot 2 mean NDVI
Handheld	0.665	0.601
Un-calibrated Sequoia data	0.307	0.156
Calibrated Sequoia data	0.682	0.582

6 Discussion

6.1 Field reflectance

The results show that with proper radiometric calibration and pre-processing the Parrot Sequoia can perform well for certain bands when estimating reflectance. For instance, the corrected images of the 5% reflectance plate were estimated with the greatest accuracy in the red band. Furthermore, all the bands could estimate the reflectance plate of the 20% reflectance plate within a 10% error span. However, this was not the case for the red and NIR band when captured at an altitude of 60 meters. This could possibly be the cause of some unknown factor that is not due to the radiometric calibration. For instance, Stark et al. (2018) show that the BRDF effect in images can produce large errors in pixel values if the field of view of the system is large – which it is on the Parrot Sequoia. Furthermore, Fernandez-Guisaraga et al. (2018) showed that the BRDF effects are highly present for the Parrot Sequoia. The argument stems in the fact that for some estimation of reflectance the estimation did not change with changes in flight altitude - as seen with the REG band for the 20 and 50% reflectance plates for instance. However, if estimated reflectance increased with flight altitude for all the bands then it could be assumed that the radiometric calibration would not be suitable images captured at higher altitude. It can be argued then that with the methodology proposed several images should be captured at each altitude as a single image can thus exhibit reflectance variability. An image should then be chosen for reflectance calculation that does not exhibit some environmental factor that will produce errors. Furthermore, with images taken at a greater altitude the pixels will represent a larger ground area resulting in pixels containing more varied spectral signatures, a mixed pixel. From this it can be argued that a lower flight altitude is recommended for the estimation of reflectance with the use of this radiometric calibration and camera system.

The NIR and REG band exhibited the lowest error in estimated reflectance for the 50% reflectance plate where the other bands had far higher error of estimated reflectance. The 99% reflectance plate could not be replicated to any degree by any band, but the green and red band produced the largest errors. These results imply that the radiometric calibration used with the Parrot Sequoia is not suitable for identifying the true reflectance of highly reflective surfaces.

The error of estimation can be misleading. For example, the error in estimated reflectance for the 5% reflectance plate in the green band was 40% while the error for the 99% reflectance plate in the REG band was 23% at a capture height of 10 meters. So, by blindly looking at the error one would assume that the estimation of the 5% reflectance plate in the green band was poor while the estimation of the 99% reflectance plate in the REG band was better. However, by looking at the actual estimated reflectance for the 99% reflectance plate in the REG band it estimated a reflectance of 77% where it

should have been 99%. This means that the estimation was off by a reflectance of 22% whereas the estimation of the 5% reflectance plate in the green band was just off by a reflectance of 1.5%. By looking at the actual estimated reflectance and not at the error, in percent, one could thus argue that the green band was better at estimating the 5% reflectance plate than the REG band was at estimating the 99% reflectance plate. This makes it hard to claim that the estimated reflectance is good or bad as in the case presented above. However, if both the error and the deviation of absolute reflectance is low one could assume that the estimation in question was accurate as with the 20% reflectance plate for the REG band. Furthermore, the accuracy of the reflectance estimations is hard to validate as finding information or literature on acceptable boundaries of reflectance estimation error could not be found. For future studies the performance could be quantified by using more radiometric calibrations, such as the empirical line method, and using reflectance plates measurements with a calibrated handheld spectrometer for comparison (Berra et al., 2017).

6.2   NDVI

The methodology for radiometric calibration and image processing provided NDVI values closer to the NDVI values calculated with the handheld spectrometer. It should be noted that central wavelengths for the red and NIR band for the Parrot Sequoia and the handheld spectrometer does not perfectly overlap. Thus, the measured NDVI should in theory not be identical as the different systems measure different wavelengths. However, without any radiometric calibration the NDVI produced was drastically lower compared to the handheld spectrometer. Thus, NDVI derived from the radiometric calibration can be argued to be more accurate compared to the un-calibrated NDVI if the handheld spectrometer is assumed to be the baseline NDVI measurement. Furthermore, the un-calibrated NDVI would imply that the vegetation was sparse at the location which was not the case. However, if a more rigorous statement is to be made more NDVI products from other systems need to be incorporated in the comparison. This could be achieved by doing the field campaign that coincides with a satellite flyover of the same area and then using the satellite data to derive NDVI for comparison (Berra et al., 2017). Furthermore, an incorporation of more plots to calculate NDVI within could also create the possibility to conduct more statistical testing such as correlations and significance between NDVI products.

The reflectance-based VI used was NDVI that utilizes the red and NIR band. The results show that the red and NIR band has some of the lowest errors in estimated reflectance. Hence, it is difficult to know how well the radiometric calibration would have impacted another reflectance-based VI that does not rely on the red and NIR band. For example, the highest errors in estimated reflectance was seen in the green band and thus the impact of this on a VI utilizing the green band is hard to predict.

Further analysis on error propagation to given VI is needed to determine if the radiometric calibration proposed is suitable for a variety of reflectance-based VI.

6.3 Radiometric calibration

The results show that with proper calibration data reflectance values close to target reflectance can be estimated. However, it is important to keep the relationship between the sunshine sensor signal and the camera pixel value linear when creating the reflectance correction matrix. For instance, by having a non-linear relationship between the sunshine sensor and camera pixel value the slope being used in the calibration can be prone to errors thus providing a bad prediction of reflectance. This can be seen in figure 8 for the green and red band where the estimated reflectance for the reflectance plate in question is outside of the possible reflectance range at the edges of the image. This is most likely due to the vignetting effect that will induce saturation of the pixel values at the edges of the images during brighter illuminated conditions. The argument stems from the fact that the area of the image prone to vignetting in the green band is also the area of the image having values outside the possible range of reflectance values. Thus, when saturation occurs of the 10-bit range of the camera but not the sunshine sensor then the relationship will not be linear at higher values. However, this pixel-by-pixel radiometric calibration was able to remove the vignetting present in the NIR and REG band as the vignetting present did not equal to a saturation of the 10-bit range of the camera. Results showed that the REG and NIR band was most accurate at estimating the target reflectance across the image possibly due to this notion.

When using the 99% calibration data to estimate the target reflectance upon an image used to derive itself the results were poor. The sheer number of pixels with values outside the possible range of reflectance values implied that the 99% reflectance calibration data was untrustworthy to use in the field campaign. The 99% reflectance plate is thus not deemed to be well suited for the radiometric calibration of the Parrot Sequoia. The problem is possibly due to the pixels being saturated for most of the images taken during the radiometric calibration run. This could be solved by decreasing the shutter speed of the camera so that less light enters the sensor hence reducing the pixel value or by doing the radiometric calibration run on a less illuminated day. However, a shorter shutter speed could result in dark images over vegetation.

The automatic settings calibration data did not produce any sensible estimations of reflectance of the 99% reflectance plate used for that calibration run. Hence, the automatic settings of the Parrot Sequoia are not deemed suitable for the estimation of reflectance of vegetation with the methodology proposed in this study.

The notion of preserving the linearity of the sunshine sensor and the pixel values for the radiometric calibration run stresses the importance for more rigorous pre-processing of the images. This means that in the images selected for the calculation the reflectance correction matrix should not have any saturation present of the 10-bit range for any of the images. In this study it would imply using a lower shutter speed for the green and red band specifically. Fernandez-Guisaraga (2018) showed similar results for the Parrot Sequoia where the green and red bands were prone to saturation and showed horizontal banding, similar to this study. However, horizontal banding seems to be handled in the same fashion as vignetting was processed by the pixel-by-pixel radiometric calibration for the NIR and REG band. Hence, the radiometric calibration method used can provide a solution to systematic noise such as banding and vignetting if careful attention is taken to the data used for the radiometric calibration run. This kind of pre-processing on a pixel-by-pixel basis can be very time consuming as each pixel would have to be checked for saturation before being used. Furthermore, Jin & Eklundh (2015) argue that if the k, derived from calibration, multiplied with the incoming radiation signal is greater than the intercept of the linear relationship then that pixel in question should not be used. This was not done in this study as that kind of pixel-by-pixel processing was to time consuming. If then a more rigorous pixel-by-pixel processing chain is adapted these problems could be solved. Thus, with this method reflectance data can be gathered that can be compared in a temporal manner that is necessary within the field of phenology.

The radiometric calibration used relies on both outgoing and incoming solar radiation. This implies that an accurate incoming solar radiation signal is crucial for the radiometric calibration to work. From the results the sunshine sensor is on par with designated multispectral sensors. As the radiometric calibration used relies on a linear relationship between the sunshine sensor and the pixel values the difference of the bit ranges can be disregarded.

6.4   Dark current and vignetting

The dark current and vignetting tests provided some insightful information on the Parrot Sequoia behaviour. The results showed that the vignetting present deviates from the vignetting defined by Kelcey & Lucieer (2012). The vignetting present in the Parrot Sequouia is not a radial decrease in pixel values, as expected, but an increase that is not radial. The vignetting present is severe for the green, red and to some extent the NIR band. The REG band show small signs of vignetting. However, it could be noted as mentioned above that the radiometric calibration can solve these issues if there is no real saturation of the 10-bit range. This was evident as the NIR and REG band after radiometric calibration presented no severe vignetting effect. Due to the vignetting being reversed with increased values towards the edges the saturation of the bit range must be minimized with a shorter shutter speed for example. Furthermore, Kelcey and Lucieer (2012) showed that decreases in shutter

speed resulted in less vignetting taken from their digital camera that could be applicable to the Parrot Sequoia. Thus, future studies could analyse the effects of different shutter speeds on the vignetting effect in the Parrot Sequoia.

The dark current tests show that the Parrot Sequoia is strongly affected by temperature. The relationship between the random noise and temperature is evident with high image mean pixel values with increased temperatures. The dark current signal, image median, does not increase in such a drastic rate with increased temperature. The dark current signal measured does not completely correspond to the cameras own dark current metric. However, to derive accurate dark current readings for a given temperature, testing would have to be done with the shutter speed to be used in the field (Mansouri et al., 2005). This was not possible due to the camera not being able capture images during dark current testing with the shutter speed selected to be used in the field campaign. This temperature dependence could imply problems when operating the Parrot Sequoia over a longer period with varying temperatures during field campaigns such as the case with phenological studies. However, the noise present in the dark current images was substantial but were at such high temperatures that might never be reached in field. It should also be noted that the ISO and shutter speed of the dark current images were far away from common values utilized in the field. This means that the temperature responses of the camera might not be as severe if dark current images can be captured with static settings.

7 Conclusion

In this study a novel pre-processing and pixel-by-pixel radiometric calibration method for images captured with the Parrot Sequoia camera was developed. The method was shown to be capable at providing accurate reflectance estimations of certain Spectralon reflectance plates with certain wavelength bands. However, some uncertainties exist as some reflectance plates are not well estimated and some bands provide larger error in estimated reflectance than others. With the radiometric calibration applied to images the calculated NDVI is closer to handheld derived NDVI. This means that this methodology can be used to derive reflectance-based vegetation indices usable for phenological studies. However, the properties of the Parrot Sequoia and the radiometric calibration used does require careful attention not to produce errors in estimated reflectance regarding saturation due to vignetting, temperature, systematic and random noise. More work is needed to better compare and evaluate the performance of the methodology presented in this study by comparing reflectance and Vis from other UAV systems.

8 References

Bachmann, F., Herbst, R., Gebbers, R., & Hafner, V. (2013). Micro UAV Based Georeferenced Ortophoto Generation in VIS+NIR for Precision Agriculture. *International Archives of the Photogrammetry, Remote Sensing and Spatial Information Sciences – ISPRS Archives*, *40*(1W2), 11-16.

Berra, E. F., Gaulton, R., & Barr, S. (2016). Use of a digital camera onboard a UAV to monitor spring phenology at individual tree level, Bejing, 2016. New Jersey, IEEE.

Berra, E. F., Gualton, R., & Barr, S. (2017). Unmanned Aerial Vehicles for Multitemporal Monitoring of Vegetation Reflectance and NDVI. *IEEE Transactions on Geoscience and Remote Sensing*, *55*(9), 4878-4886.

Bueren, S. K., Burkart, A., Huen, A., Rascher, U., Tuohy, M. P., & Yule, I. J. (2015). Deploying four optical UAV-based sensors over grassland: challenges and limitations. *Biogeosciences*, *12*, 163-175.

Burkart, A., Hecht, V. L., Kraska, T., & Rascher, U. (2018). Phenological analysis of unmanned aerial vehicle based time series of barley imagery with high temporal resolution. *Precision Agriculture*, *19*, 134-146.

Chuvieco, E. (2016). *Fundamentals of Satellite Remote Sensing: an environmental approach*. United States, Florida, Boca Raton: Taylor & Francis Group.

Fernandez-Guisuraga, J. M., Sanz-Ablenado, E., Suarez-Seoane, S., & Calvo, L. (2018). Using Unmanned Aerial Vehicles in Postfire Vegetation Suurvey Campaings through Large and Heterogeneous Areas: Oppurtunities and Challenges. *Sensors*, *18*, 1-17.

Gao, B. C., Davis, C., & Goetz, A. (2006). A Review of Atmospheric Correction Techniques for Hyperspectral Remote Sensing of Land Surfaces and Ocear Color. *2006 IEEE International Symposium on Geoscience and Remote Sensing*, *2006*, 1979-1981.

Jin, H. & Eklundh, L. (2015). In Situ Calibration of Light Sensors for Long-Term Monitoring of Vegetation. *IEEE Transactions on Geoscience and Remote Sensing*, *53*(6), 3405-3416.

Kelcey, J. & Lucieer, A. (2012). Sensor Correction of a 6-Band Multispectral Imaging Sensor for UAV Remote Sensing. *Remote Sensing*, *4*, 1462-1493.

Klosterman, S., & Richardson, A. D. (2017). Observing spring and fall phenology in a Deciduous Forest with Aerial Drone Imagery. *Sensors,* 17, 1-17.

Klosterman, S., Melaas, E., Wang, J. A., Martinez, A., Frederick, S., O'Keefe, J., … & Richardson, A. D. (2018). Fine-scale perspectives on landscape phenology from unmanned aerial vehicle (UAV) photography. *Agricultural and Forest Meteorology*, *248*, 397-407.

Mansouri, A., Marzani, F. S., & Gouton, P. (2005). Development of a protocol for CCD calibration: Application to a multispectral imaging system. *Internation Journal of Robotics and Automation, 20*(2), 94-100.

Mullikin , J. C., van Vliet, L. J., Netten, H., Bodekke, F. R., vad der Feltz, G., & Young, I. T. (1994). Methods for CCD camera characterization. *1994 International Symposium on Electronic Imaging: Science and Technology*, 1994, 73-84.

Rasmussen, J., Ntakos, G., Nielsen, J., Svensgaard, J., Poulsen, R. N., & Christensen, S. (2016). Are vegetation indices derived from consumer-grade cameras mounted on UAVs sufficiently reliable for assessing experimental plots?. *European Journal of Agronomy*, *74*, 75-92.

Richards, J. A., & Jia, X. (2006). *Remote Sensing Digital Image Analysis*. Germany, Heidelberg, Berlin: Springer-verlag.

Smith, G, M. & Milton, E, J. (1999). The use of the empirical line method to calibrate remotely sensed data to reflectance. *International Journal of Remote Sensing*, *20*(13), 2653-2662.

Stark, B., Zhao, T., & Chen Y. (2018). An Analysis of the Effect of the Bidirectional Reflectance Distribution Function on Remote Sensing Imagery Accuracy from Small Unmanned Aircraft Systems. *2016 International Conference on Unmanned Aircraft Systems (ICUAS)*, *2016*, 1342-1350.

Soumalainen, J., Anders, N., Iqbal, S., Roerink, G., Franke, J., Wenting, P., … & Kooistra, L. (2014). A Lightweight Hyperspectral Mapping System and Photogrammetric Processing Chain for Unmanned Aerial Vehicles. *Remote Sensing*, *6*, 11013-11030.

Xue, J. & Su, B. (2017). Significant Remote Sensing Vegetation Indices: A Review of Developments and Applications. *Journal of Sensors*, *2017*, 1-17.

Yang, G., Liu, J., Zhao, C., Li, Z., Huang, Y., Yu, H., … Yang, H. (2017). Unmanned Aerial Vehicle Remote Sensing for Field-Based Crop Phenotyping: Current Status and Perspectives. *Frontiers in Plant Science*, *8*, 1-26.

Zhang, H., Huang, M., Qing, X., Li, G., & Tian, C. (2017). Bibliometric Analysis of Global Remote Sensing Research during 2010-2015. *International Journal of Geo-Information*, *6*(11), 1-19.